Nano Research

Open Access

Research Article

Synergistic regulation of donor–acceptor aggregation and morphology by isomeric solid additives for high-performance organic solar cells with over 20% efficiency

Zhiyi Zhao[1,§], Dipeng Ren[2,§], Ruimin Zhou[1] ✉, Hui Wang[1], Zhen Wang[3], Jianqi Zhang[4], Dan Deng[4], Yanlin Song[5], and Zhixiang Wei[4,6] ✉

[1] *College of Chemistry, Zhengzhou University, Zhengzhou 450001, China*
[2] *School of Electrical and Information Engineering, Zhengzhou University, Zhengzhou 450001, China*
[3] *Hangzhou International Innovation Institute, Beihang University, Hangzhou 311115, China*
[4] *Key Laboratory of Nanosystem and Hierarchical Fabrication of Chinese Academy of Sciences, National Center for Nanoscience and Technology, Beijing 100190, China*
[5] *Key Laboratory of Green Printing, Institute of Chemistry, Chinese Academy of Sciences (ICCAS), Beijing Engineering Research Center of Nanomaterials for Green Printing Technology, National Laboratory for Molecular Sciences (BNLMS), Beijing 100190, China*
[6] *University of Chinese Academy of Sciences, Beijing 100049, China*
[§] *Zhiyi Zhao and Dipeng Ren contributed equally to this work.*

Cite this article: *Nano Research*, **2026**, *19*, 94908417. https://doi.org/10.26599/NR.2026.94908417

ABSTRACT: Molecular aggregation and phase morphology of the active layer in bulk-heterojunction (BHJ) solar cells are crucial to attain efficient and stable organic solar cells (OSCs). Most studies of solid additives in high-efficiency OSCs have primarily focused on the impact of these additives on the acceptors, while largely neglecting the synergistic effects of additives on donor and acceptor. Herein, we introduce a synergistic morphology regulation approach by utilizing two isomeric solid additives (4-bromobenzothiadiazole (4-BBT) and 5-bromobenzothiadiazole (5-BBT)). 4-BBT or 5-BBT promotes both the crystallinity and π–π stacking of the polymer donor PM6 while effectively suppressing excessive aggregation of the acceptor L8-BO, which leads to a favorable phase morphology. When mixed additives are loaded simultaneously, synergistic regulation can be achieved, enabling finer nanoscale phase separation with enhanced donor–acceptor miscibility and well-ordered packing. Further analyses indicate that the mixed additives effectively slow down the film formation and charge relaxation dynamics, thereby prolonging crystallization time and enhancing π–π stacking while effectively suppressing recombination losses. Consequently, modified by the mixed additives, the PM6:L8-BO device demonstrates high efficiency of 19.32%, coupled with improved short-circuit current (J_{SC}) and fill factor (FF). Besides, the D18:L8-BO-C4-based devices treated with 4-BBT+5-BBT delivered a remarkable efficiency of 20.13%, with an outstanding FF of 83.01%. Furthermore, the optimized device shows excellent photostability and thermal stability. This study provides a versatile and effective strategy for accurate regulation of the molecular aggregation and phase morphology through synergistic isomeric solid additive engineering, thereby offering insights into the rational design of efficient and stable organic photovoltaic materials.

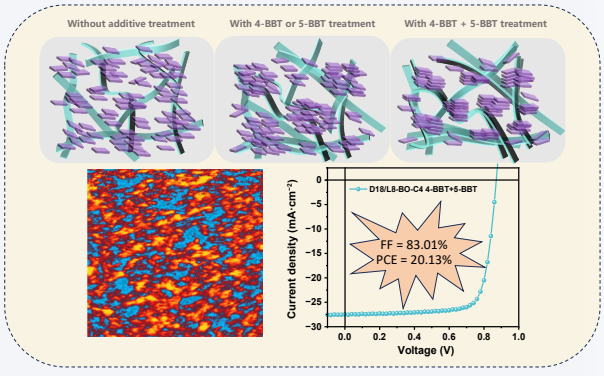

KEYWORDS: organic solar cells, isomeric solid additives, morphology regulation, molecule aggregation, film-formation dynamics

1 Introduction

Organic solar cells (OSCs) have emerged as a promising renewable energy technology due to their light weight, flexibility, and processability in solution [1–7]. Recent breakthroughs of non-fullerene acceptors (NFAs), particularly the Y6-series, led to OSCs on the verge of practical implementation with power conversion

Received: November 18, 2025; **Revised:** January 2, 2026
Accepted: January 7, 2026

✉Address correspondence to Ruimin Zhou, zhourm@zzu.edu.cn; Zhixiang Wei, weizx@nanoctr.cn

efficiencies (PCEs) over 20% [8–12]. However, the device performance and stability of OSCs are mainly driven by the molecular aggregation and phase morphology of the bulk-heterojunction (BHJ) active layer, where the charge generation, transport, and recombination are being dominated by either molecular packing, crystallinity, and phase separation [13–21]. Hence, achieving fine control over molecular packing and phase morphology remains a central challenge for realizing both high efficiency and long-term stability [22–24].

Various additive engineering strategies have been devised to achieve molecular packing optimization of the OSCs film morphology, including solvent additives, volatile solid additives, and polymer compatibilizers [25–29]. Although solvent additives (e.g., 1,8-diiodooctane (DIO) and 1-chloronaphthalene (CN)) could effectively adjust phase separation during film formation, due to their high volatility and environmental toxicity, they would not lead to various reproducibility and large-scale processing [25, 30–32]. Solid additives take another route, where controlled molecular interactions can regulate the device morphology in a more controllable and environmentally friendly way [33–37]. However, most of the reported solid additives behave unilaterally (i.e., doping at donors' crystallinity or acceptors' aggregation), thereby promoting select components at the expense of the other, leading to inefficiencies in all components resulting in the non-ideal phase morphology, and consequently, the non-optimal device performance [38–42].

In order to overcome above limitations, we report a pair of isomeric solid additives, 4-bromobenzothiadiazole (4-BBT) and 5-bromobenzothiadiazole (5-BBT), containing the same chemical backbone, but different substitution sites. The two families exhibit distinct synergistic interaction with donor and acceptor molecules, enabling the selective achievement of synergistic morphology regulation [43–45]. In particular, 4-BBT or 5-BBT promotes the crystallinity and π–π stacking of the polymer donor PM6 while effectively suppressing excessive aggregation of the acceptor L8-BO, achieving favorable phase morphology. The combinations, in compound-additive couples (4-BBT+5-BBT), bring balanced aggregation, the refined phase separation, and enhanced donor–acceptor miscibility, suggesting synergistic maturation during device operation, which can further contribute to optimized pathways for charge generation and transport, achieving ultimately superior photovoltaic performances and improved device stabilities. Transient absorption (TA) and optoelectronic analyses confirm enhanced charge dissociation and suppressed recombination, achieving a high PCE of 19.3% with superior stability. Besides, upon treatment with 4-BBT+5-BBT additive, the D18:L8-BO-C4-based devices delivered a remarkable PCE of 20.13%, with an outstanding fill factor (FF) of 83.01%. This study not only provides fundamental insights into isomeric additive synergy but also establishes a generalizable strategy for morphology engineering toward efficient and durable organic photovoltaic devices.

2 Results and discussion

Figure 1(a) shows the chemical structures of PM6, L8-BO, and the solid additives (4-BBT and 5-BBT). The energy level alignment (Fig. 1(b)) indicates that the highest occupied molecular orbital (HOMO)/lowest unoccupied molecular orbital (LUMO) offsets between PM6 and L8-BO are in an appropriate balance state for achieving good charge transfer. To study the volatility of the two isomer solid additives, the derivatives were recorded by thermogravimetric analysis (TGA). In Fig. 1(c), it can be found that all the isomer solid additives possess favorable volatile properties. Compared to 5-BBT (5% weight loss, 98.7 °C), 4-BBT showed slightly higher T_d of decomposition temperature (5% weight loss, 104.08 °C).

Figure 1(d) shows the ultraviolet–visible (UV–Vis) absorption profiles of PM6 films with or without isomer solid additive treatments. Compared to the as-cast PM6 film (616 nm), the solid additive-treated PM6 films exhibit slightly red-shifted profiles and intensified 0–0 vibronic peak with a maximum absorption wavelength of approximately 622 nm. This suggests enhanced π–π stacking interactions and improved molecular ordering, ultimately leading to enhanced donor aggregation. Figure 1(e) presents the normalized UV–Vis absorption spectra of neat L8-BO films and those processed with the additive 4-BBT, 5-BBT, and 4-BBT+5-BBT system. All films exhibit strong absorption in the near-infrared (NIR) region. Upon additive incorporation, the main absorption peak shows a slight blue shift from 795 nm (pristine film) to 790–794 nm. Typically, the A_{0-0}/A_{0-1} (A_{0-0} represents the intensity of the 0–0 peak in the UV–Vis fitting spectrum and A_{0-1} denotes the intensity of the 0–1 peak in the UV–Vis fitting spectrum) ratio is employed to evaluate the extent of molecular aggregation, whereas the $FWHM_{0-0}/FWHM_{0-1}$ (FWHM: full width at half maximum) ratio reflects the degree of molecular ordering [22, 25]. The corresponding parameters are summarized in Table S1 in the Electronic Supplementary Material (ESM). The fitted UV–Vis spectra of without or with additives are integrated in Fig. S3 in the ESM about neat L8-BO films. Compared with the pristine L8-BO film (2.97), the A_{0-0}/A_{0-1} ratios of L8-BO:4-BBT and L8-BO:5-BBT decrease significantly to 2.57 and 2.39, respectively, indicating weakened J-type aggregation. Notably, the binary-additive-treated L8-BO:4-BBT+5-BBT exhibits a further reduced value of 2.11, suggesting a synergistic suppression of aggregation. Meanwhile, the $FWHM_{0-0}/FWHM_{0-1}$ ratios of the single-additive-treated films (1.71 and 1.64) are lower than that of the pristine L8-BO film (1.97), implying enhanced molecular ordering. This trend becomes more pronounced in the binary-additive-treated film, where the ratio further decreases to 1.42, confirming a cooperative effect in promoting molecular order. Moreover, the binary-additive film possesses a steeper absorption edge, which typically manifests as an enhancement in crystallinity. Hence, compared with single-additive treatment, the simultaneous application of 4-BBT and 5-BBT can more effectively inhibit excessive aggregation and further enhance the molecular order and crystallinity degrees, thus enabling more precise modulation of active layer morphology. The normalized UV–Vis absorption spectra for the blend films are illustrated in Fig. 1(f), indicating high conformity with those of the counterpart neat films.

To assess the miscibility between donor and acceptor components, contact angle measurements were conducted to derive Flory–Huggins interaction parameter (χ) (Figs. S1 and S2 in the ESM, and Fig. 1(g) and Table S2 in the ESM). For pristine PM6:L8-BO blend, χ value was estimated to equal to 0.30, signifying slight lack of high degree mutual homogeneous compatibility, while by doping single additive, χ decreased to 0.26 (4-BBT) and 0.29 (5-BBT), indicating a pronounced compatibility state. More markedly, the obtained χ value of the binary-additive-treated system reached the lowest value of 0.25, which suggested a synergistic effect occurred in the donors–acceptors interaction process. Such improved miscibility is expected to facilitate a more favorable phase distribution and thereby contribute to optimized blend morphology, as discussed in the subsequent section.

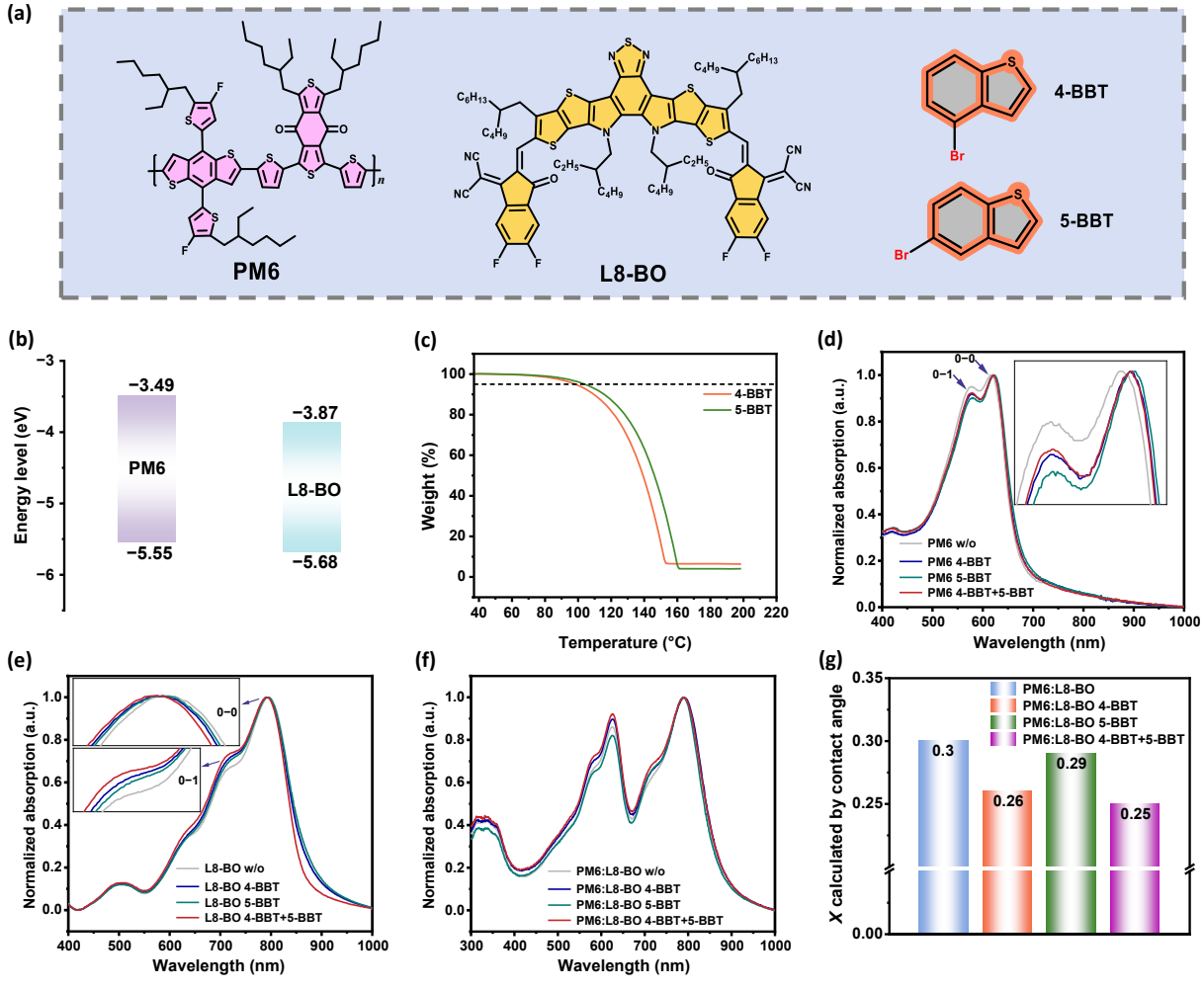

Figure 1 (a) Chemical structures of PM6, L8-BO, 4-BBT, and 5-BBT. (b) Energy level diagrams of PM6 and L8-BO. (c) TGA curves of additives. ((d)–(f)) UV–Vis absorption spectra of neat and blend films. (g) Calculated Flory–Huggins parameters with different additives.

To investigate the impact of 4-BBT, 5-BBT, and dual additive 4-BBT+5-BBT regulation of the donor–acceptor aggregation on the photovoltaic performance, OSCs were fabricated using conventional device architecture for BHJ (glass/indium-tin oxide (ITO)/poly(3,4-ethylenedioxythiophene):polystyrenesulfonic acid (PEDOT:PSS)/PM6:L8-BO/PFN-Br/Ag). The detailed device fabrication procedures are provided in the ESM. After optimization, the optimal PM6:L8-BO device processed with 4-BBT employed a 4-BBT concentration of 10 mg·mL^{-1}, while the optimal device processed with 5-BBT used a 5-BBT concentration of 10 mg·mL^{-1}. For the PM6:L8-BO device processed with the mixed additive system, both 4-BBT and 5-BBT were applied at concentrations of 10 mg·mL^{-1}. In addition, the key photovoltaic parameters are summarized in Table 1, with the corresponding short-circuit current density–voltage (J–V) curves in Fig. 2(a). It can be seen that the PM6:L8-BO device exhibits a relatively low PCE of 16.51%, with the FF of 72.97%, short-circuit current (J_{SC}) of 24.55 mA·cm^{-2}, and open-circuit voltage (V_{OC}) of 0.922 V, owing to the significant self-aggregation of L8-BO. Then, by introducing 4-BBT, the inhibited aggregation of L8-BO led to an increase in the FF from 72.97% to 77.21%, resulting in an enhanced PCE of 17.67%. Next, with the introduction of 5-BBT, the resulting device shows a higher FF of 77.04% and an improved J_{SC} of 25.85 mA·cm^{-2}, thus achieving a PCE of 17.96%. Finally, with the further introduction of 4-BBT+5-BBT, the resulting device not only shows a further increase in FF to 79.39%, but also a higher J_{SC} of 27.32 mA·cm^{-2}, ultimately achieving a PCE of 19.32%. The associated external quantum efficiency (EQE) spectra are shown in Fig. 2(b), from which it can be seen that the deviation between the integrated J_{SC} (J_{cal}) from EQE and the J_{SC} obtained from J–V measurements is within 5%, demonstrating the reliability of our device performance.

To delve deeper into the charge recombination dynamics, the dependence of V_{OC} and J_{SC} on light intensity (P_{light}) was studied, as shown in Figs. 2(c) and 2(d), the relationship between V_{OC} and P_{light} can be described as $V_{OC} \propto n(k_B T/q) \ln P_{light}$ (where n is carrier concentration, k_B is Boltzmann constant, T is the Kelvin temperature, and q is the elementary charge). The slope of V_{OC} versus $\ln(P_{light})$ indicates the recombination type, a slope of $k_B T/q$ implies that bimolecular recombination is the predominant recombination mechanism, and $2k_B T/q$ suggests that monomolecular recombination (trap-assisted recombination or Shockley–Read–Hall recombination) is the dominant recombination mechanism [46, 47]. The datum of n closer to 1 means less trap-assisted recombination in the OSCs. The n values of the devices processed without additive, 4-BBT, 5-BBT, and 4-BBT+5-BBT additives are 1.09, 1.07, 1.12, and 1.05, respectively (Fig. 2(d)). The smaller slope value observed for the dual-additive device indicates that monomolecular recombination at trap centers

Table 1 Photovoltaic parameters of the OSCs on blend films processed with or without additives

Active layer	V_{OC} (V)	J_{SC} (mA·cm^{-2})	J_{cal} (mA·cm^{-2})	FF (%)	PCE (%)[a]
PM6:L8-BO	0.922	24.55	24.23	72.97	16.51 (16.50 ± 0.06)
PM6:L8-BO 4-BBT	0.910	25.14	25.05	77.21	17.67 (17.60 ± 0.08)
PM6:L8-BO 5-BBT	0.902	25.85	25.68	77.04	17.96 (17.83 ± 0.04)
PM6:L8-BO 4-BBT+5-BBT	0.891	27.32	26.51	79.39	19.32 (19.31 ± 0.01)
D18:L8-BO-C4 4-BBT+5-BBT[b]	0.881	27.53	26.82	83.01	20.13 (20.10 ± 0.02)

[a]Average values and standard deviations are obtained from more than 10 devices. [b]Using [2-(9H-carbazol-9-yl)ethyl]phosphonic acid (2PACz) as hole-transport layer (HTL).

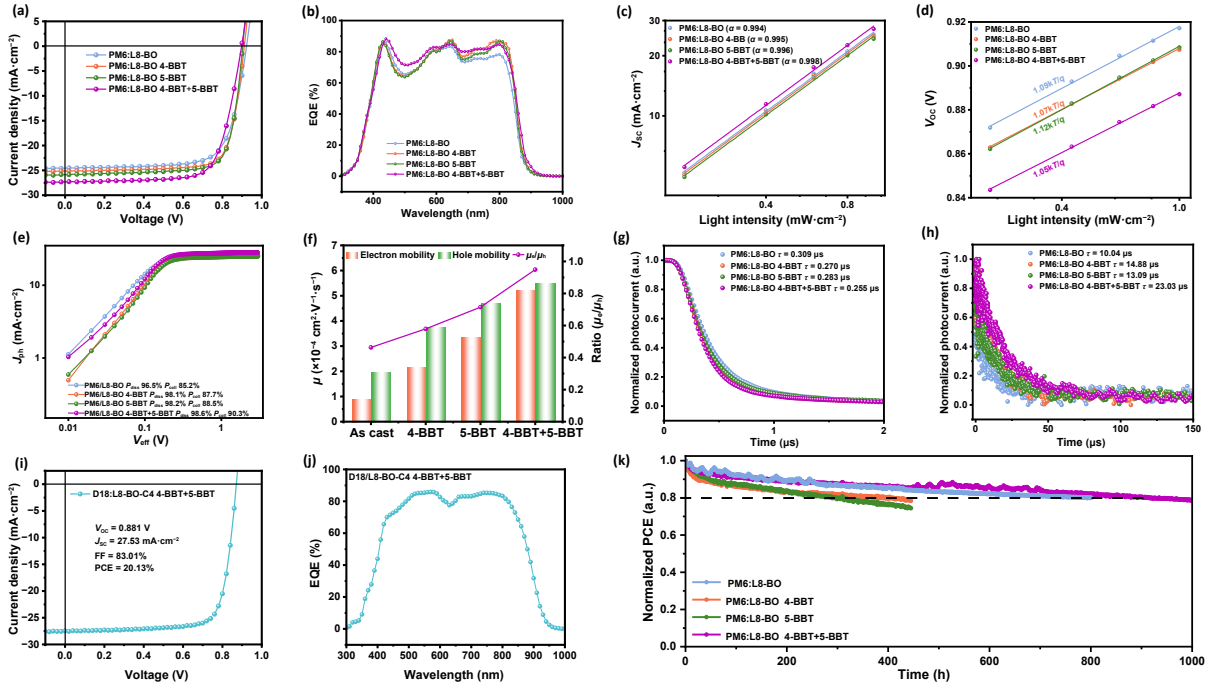

Figure 2 (a) *J*–*V* curves of the PM6:L8-BO-based devices without or with solid additive treatments (4-BBT, 5-BBT, and 4-BBT+5-BBT). (b) EQE curves of the corresponding PM6:L8-BO-based OSCs. (c) Dependence of J_{SC} on light intensity of the corresponding devices. (d) Dependence of V_{OC} on light intensity of the corresponding devices. (e) J_{ph} versus V_{eff} of the corresponding devices. (f) Charge mobilities of the PM6:L8-BO-based blend films without or with solid additive treatments (4-BBT, 5-BBT, and 4-BBT+5-BBT). (g) Normalized TPC and (h) TPV of devices fabricated with or without additives. (i) *J*–*V* curve of the D18:L8-BO-C4-based devices with 4-BBT+5-BBT treatment. (j) EQE curve of the corresponding D18:L8-BO-C4-based OSCs. (k) Unencapsulated devices under maximum power point (MPP) tracking with continuous illumination (100 mW·cm^{-2}) in an N_2 atmosphere.

is reduced, reflecting a decrease in trap-assisted recombination. This reduction contributes to the improved FF, which is consistent with the enhanced charge transport and extraction.

There exists a power-law relationship between J_{SC} and P_{light}. $J_{SC} \propto P_{light}\alpha$, α represents the bimolecular recombination coefficient. In the case of serious bimolecular recombination in OSCs, α is < 1, and if there is no bimolecular recombination, α should be 1. As shown in Fig. 2(c), the devices processed without additive, 4-BBT, 5-BBT, and 4-BBT+5-BBT additives show α values of 0.994, 0.995, 0.996, and 0.998, respectively. The device treated with 4-BBT and 5-BBT exhibits a slightly higher α value, suggesting reduced losses due to bimolecular recombination.

The exciton production rate and charge transfer probability were studied by analyzing the relationship between net photocurrent density ($J_{ph} = J_{Light} - J_{Dark}$) and effective voltage ($V_{eff} = V_0 - V_{app}$), where J_{Light} is the photocurrent density, J_{Dark} is the dark current density, V_0 represents the effective voltage at which J_{ph} equals zero, and V_{app} denotes the applied bias. Typically, the exciton dissociation efficiency (P_{diss}) and charge collection efficiency (P_{coll}) are estimated from the ratios of J_{SC} to J_{sat} and J_{max} to J_{sat}, respectively, where J_{sat} is the saturation photocurrent, and J_{SC} and J_{max} correspond to the photocurrent densities under short-circuit and maximum power conditions. Related parameters are shown in Fig. 2(e). The calculated P_{diss} values are 98.1% and 98.2% for the 4-BBT and 5-BBT devices, respectively, and the corresponding P_{coll} values are 87.5% and 88.5%, respectively. The superior P_{diss} (98.6%) and P_{coll} (90.3%) indicate that the 4-BBT+5-BBT dual additives enhance the exciton dissociation efficiency and charge transport performance. This improvement is likely due to the increased donor/acceptor (D/A) interpenetrated region in the active layer. Moreover, the ordered molecular packing and shortened π–π stacking effectively facilitate charge collection, contributing to the high J_{SC} and FF values of the device.

Subsequently, space charge limited current (SCLC) method was applied to evaluate hole mobilities (μ_h) and electron mobilities (μ_e) of the PM6/L8-BO films. Apparently, the improved PCEs resulting from the 4-BBT and 5-BBT dual additives treatment are primarily attributed to the significantly higher FFs, and the high FF in the

device must originate from the improved charge transport and recombination dynamics. Therefore, we measured the hole (μ_h) and electron (μ_e) mobilities of the PM6:L8-BO blend films using SCLC method to investigate the impact of additive treatment on the charge transport properties. As shown in Fig. 2(f) and Table S7 in the ESM, the μ_h of as cast, 4-BBT, 5-BBT, and 4-BBT+5-BBT processed blend devices are 1.987×10^{-4}, 3.777×10^{-4}, 4.716×10^{-4}, and 5.524×10^{-4}, respectively. The μ_e of the corresponding devices are 9.205×10^{-5}, 2.187×10^{-4}, 3.371×10^{-4}, and 5.241×10^{-4}, respectively. In particular, the μ_e and μ_h ratio of dual additives device was the most balanced. These results indicate that the dual additives provide better charge transport, and the low recombination led to the high J_{SC} and FF.

To further investigate the carrier dynamics of OSCs, we carried out time-resolved optoelectronic studies to probe the carrier dynamics, such as charge extraction efficiency, carrier lifetimes, and recombination characteristics. The charge extraction time was evaluated under short-circuit conditions through transient photocurrent (TPC) measurements. The current decay was fitted using a mono-exponential decay model, and the resulting curves are plotted in Fig. 2(g). According to the measurement results, the charge extraction times were 0.309, 0.270, 0.283, and 0.255 μs for the PM6:L8-BO, PM6:L8-BO (4-BBT), PM6:L8-BO (5-BBT), and PM6:L8-BO (4-BBT+5-BBT) devices, respectively. These results indicate that, in the devices optimized with the dual additives, the photogenerated charges can be extracted more efficiently prior to recombination.

Meanwhile, under open-circuit voltage conditions, the decay of the transient photovoltage (TPV) can be used to determine the carrier lifetime of the device. As illustrated in Fig. 2(h), the lifetimes of the PM6:L8-BO, PM6:L8-BO (4-BBT), PM6:L8-BO (5-BBT), and PM6:L8-BO (4-BBT+5-BBT) devices are 1.93, 14.88, 13.09, and 23.03 μs, respectively. These findings demonstrate a reduced level of charge recombination in the PM6:L8-BO (4-BBT+5-BBT). Therefore, the treatment with dual additives enhances charge transport and extraction efficiency while suppressing charge recombination in PM6:L8-BO devices, thereby leading to higher J_{SC} and FF. More impressively, the D18:L8-BO-C4-based binary OSCs treated with 4-BBT+5-BBT additive treatment delivered a remarkable PCE of 20.13%, with an outstanding FF of 83.01%, as shown in Figs. 2(i) and 2(j). The chemical structure of L8-BO-C4 is shown in Fig. S4 in the ESM. To evaluate the device reliability, we systematically examined both the light-soaking stability and thermal stability of the PM6:L8-BO solar cells under different additive conditions (Fig. 2(k)). The device without any additive exhibited a quick decay in performance as the T_{80} lifetime was 801 h with continuous light (T_{80} represents the time when the device efficiency drops to 80% of the original), while the straightforward plus method of adding additive 4-BBT or additive 5-BBT individually resulted in shorter stability, with the T_{80} of these devices being 395 and 297 h, respectively. However, the device processed with the binary additive (4-BBT+5-BBT) was obtained from the results as the most operationally robust device, yielding T_{80} with 926 h under continuously illuminated conditions. The similar trend was also found under the thermal test (Fig. S5 in the ESM). The control device maintained T_{80} by heating at the temperature of 80 °C for 71.9 h; moreover, our devices with additive (4-BBT+5-BBT) kept T_{80} for 152 h, indicating its actual thermal stability superiority. Through all these clearly demonstrated results, we convincingly articulate that the alliance of these two isomeric additives can effectively restrain degradations under both photo and thermal stresses, which is also responsible for its superior device longevity.

In order to understand the relationship between structural changes in the solid additives molecules and resulting photovoltaic behavior, morphological property investigation of as-fabricated neat polymer donor, acceptor, and blend film under various additive treatment conditions was performed, utilizing grazing-incidence wide-angle X-ray scattering (GIWAXS) measurements and atomic force microscopy (AFM). Figures 3(a) and 3(b) show the two-dimensional (2D)-GIWAXS patterns of neat PM6 and L8-BO films, respectively, in both as-cast and solid additive-treated conditions. Figure S6 in the ESM presents the corresponding one-dimensional (1D) profiles. Figures 3(e) and 3(f) and Tables S3 and S4 in the ESM summarize the detailed GIWAXS parameters. All single-component PM6 and L8-BO films exhibited predominantly face-on molecular stacking orientations. For the π–π stacking peaks in neat PM6 films, the as-cast film showed *d*-spacing and coherence length (CCL) values of 3.90 and 11.13 Å, respectively. Upon introducing the isomer solid additives, the π–π stacking peaks displayed decreased *d*-spacing (3.84 Å for 4-BBT, 3.84 Å for 5-BBT, and 3.83 Å for 4-BBT+5-BBT), accompanied by significantly enhanced CCL values (14.31 Å for 4-BBT, 13.69 Å for 5-BBT, and 15.92 Å for 4-BBT+5-BBT). Similar results could also be obtained for the lamellar stacking peaks of neat PM6 films, the CCL values measured to be 53.85, 81.95, 83.15, and 86.99 Å for as-cast, 4-BBT, 5-BBT, and 4-BBT+5-BBT treated PM6 films, respectively. These results indicate that the isomer solid additives could promote tighter molecular stacking and improve crystallinity of PM6 molecules. Further, it is also noted among the PM6 films treated with solid additive treatments, the films treated with 4-BBT+5-BBT showed the smallest π–π *d*-spacing-distance as well as the highest CCL value, which indicates a higher potential to better enhance the molecular packing and the crystallinity of PM6. For the π–π stacking peaks in neat L8-BO films, the as-cast film showed *d*-spacing and CCL values of 3.78 and 13.92 Å, respectively. Upon introducing the isomer solid additives, the π–π stacking peaks displayed decreased *d*-spacing (3.76 Å for 4-BBT, 3.74 Å for 5-BBT, and 3.73 Å for 4-BBT+5-BBT), accompanied by significantly enhanced CCL values (15.32 Å for 4-BBT, 16.15 Å for 5-BBT, and 16.68 Å for 4-BBT+5-BBT). Likewise, results could be earned for the lamellar stacking peaks of neat L8-BO films, CCL values that were calculated to be equal to 30.73, 30.90, 31.76, and 32.31 Å for the as-cast, 4-BBT, 5-BBT, and 4-BBT+5-BBT treated L8-BO films, respectively. Such a result indicates that these isomer solid additives could cause tighter molecular stacking behavior to result in enhancement in the crystallinity of these L8-BO molecules to a significant extent. In addition, it is noted that among the variations of L8-BO-treated films that have undergone mixed solid additive treatments, the films that were given the 4-BBT+5-BBT treatment seem to reach the smallest π–π *d*-spacing distance, which suggests additionally greater capacity to act on L8-BO's molecular packing just to give a better crystallinity. It demonstrates that mixed isomeric solid additives could synergistically modulate the packing and crystallinity of both donors and acceptors.

Figures 3(c) and 3(d) display the AFM topography of single-component PM6 and L8-BO films with various treatments. For the PM6 films subjected to different treatments, all AFM topography images exhibit relatively smooth characteristics. Among them, the films treated with 4-BBT+5-BBT display more pronounced aggregation features. The corresponding root-mean-square (RMS)

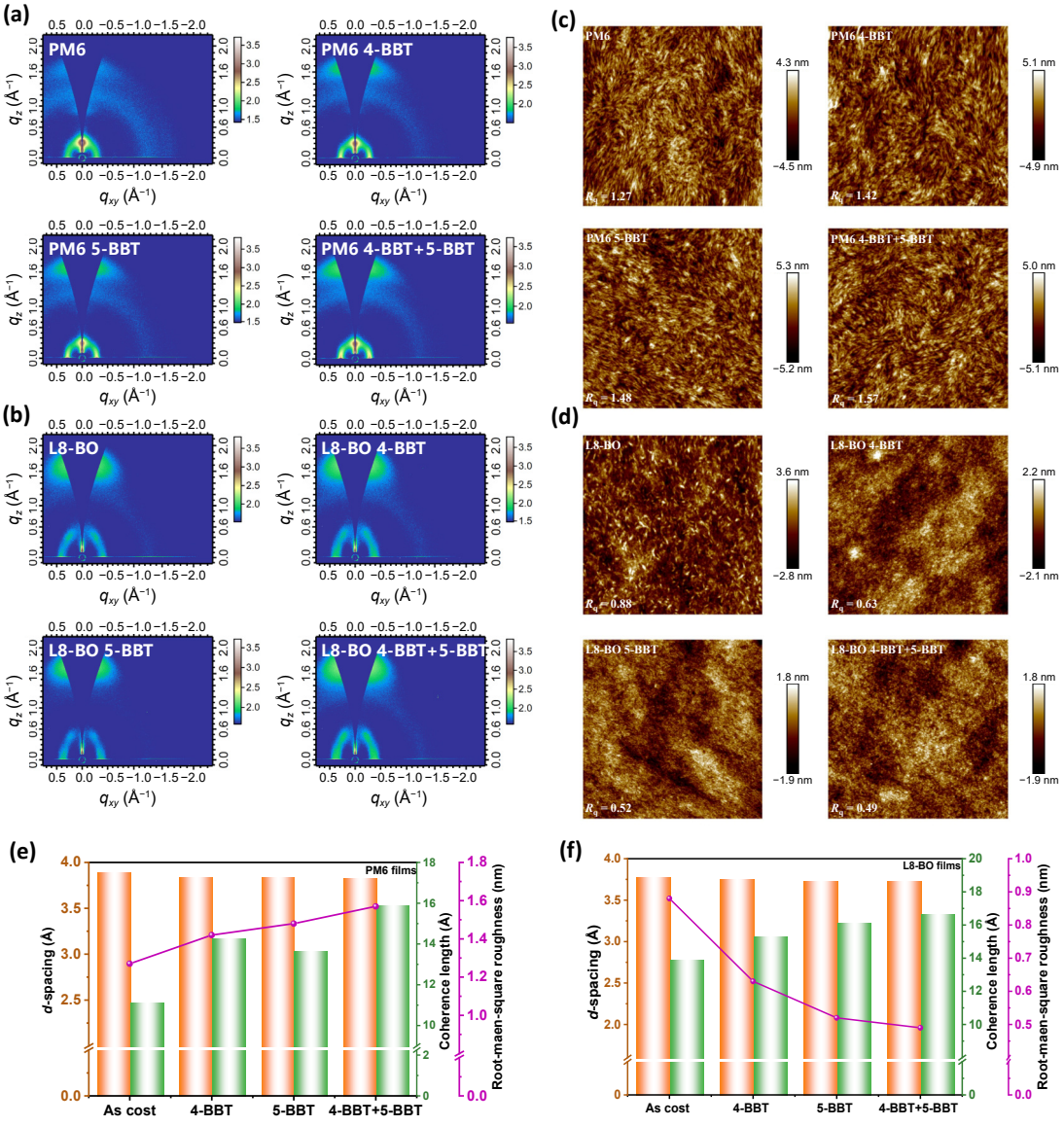

Figure 3 ((a) and (b)) 2D-GIWAXS patterns of the single-component films without (as-cast) or with solid additive treatments (4-BBT, 5-BBT, and 4-BBT+5-BBT): (a) PM6 and (b) L8-BO. ((c) and (d)) AFM images of the corresponding single-component films without (as-cast) or with solid additive treatments (4-BBT, 5-BBT, and 4-BBT+5-BBT): (c) PM6 and (d) L8-BO. ((e) and (f)) Corresponding *d*-spacing, CCL, and RMS values for the single-component films: (e) PM6 and (f) L8-BO.

values are measured to be 1.27, 1.42, 1.48, and 1.57 nm for PM6 films with as-cast, 4-BBT, 5-BBT, and 4-BBT+5-BBT treatments, respectively. The PM6 films processed with 4-BBT+5-BBT exhibited the largest RMS value, suggesting a superior ability to enhance the PM6 molecular aggregation. In contrast to PM6 films, significantly decreased aggregations were observed in L8-BO films treated with solid additives. The RMS values are measured to be 0.88, 0.63, 0.52, and 0.49 nm for L8-BO films with as-cast, 4-BBT, 5-BBT, and 4-BBT+5-BBT treatments, respectively.

The morphological features of the blend films under different additive treatments were systematically investigated via GIWAXS and AFM-IR measurements. Figure 4(a) exhibits the 2D GIWAXS diffraction patterns of PM6:L8-BO-based blend films, without (as cast) or with solid additive treatments, and the corresponding 1D profiles are depicted in Fig. 4(b). Table S5 in the ESM summarizes the detailed GIWAXS parameters. All the PM6:L8-BO blend films exhibit a face-on orientation with a regular diffraction halo in the out-of-plane (OOP) direction, which is beneficial for the charge transport. It is worth noting that, for both π–π stacking and lamellar stacking diffractions, the diffraction peaks of PM6 are so close to those of L8-BO that they cannot be clearly distinguished in the blend films. Figures 4(d) and 4(e) summarize the *d*-spacing and CCL values estimated from the out-of-plane (100) diffraction and in-plane (IP) (010) diffraction, respectively. For π–π stacking, compared to as-cast films, the blend films treated with solid additives exhibit smaller *d*-spacing and longer CCL values. Notably, the 4-BBT+5-BBT processed blends demonstrate the smallest *d*-spacing of 3.73 Å, compared to the films processed with 4-BBT and 5-BBT. For the lamellar stacking, compared to as-cast films, the blend films treated with solid additives exhibit longer *d*-spacing and longer CCL values. Although the binary-additive-processed blends show a longer *d*-spacing distance, they demonstrate the longest CCL value of 76.42 Å. These results indicate that the 4-BBT+5-BBT processed blends exhibit denser and more ordered molecular stacking and stronger crystallinity compared to the films processed with 4-BBT and 5-BBT. This finding is consistent with the

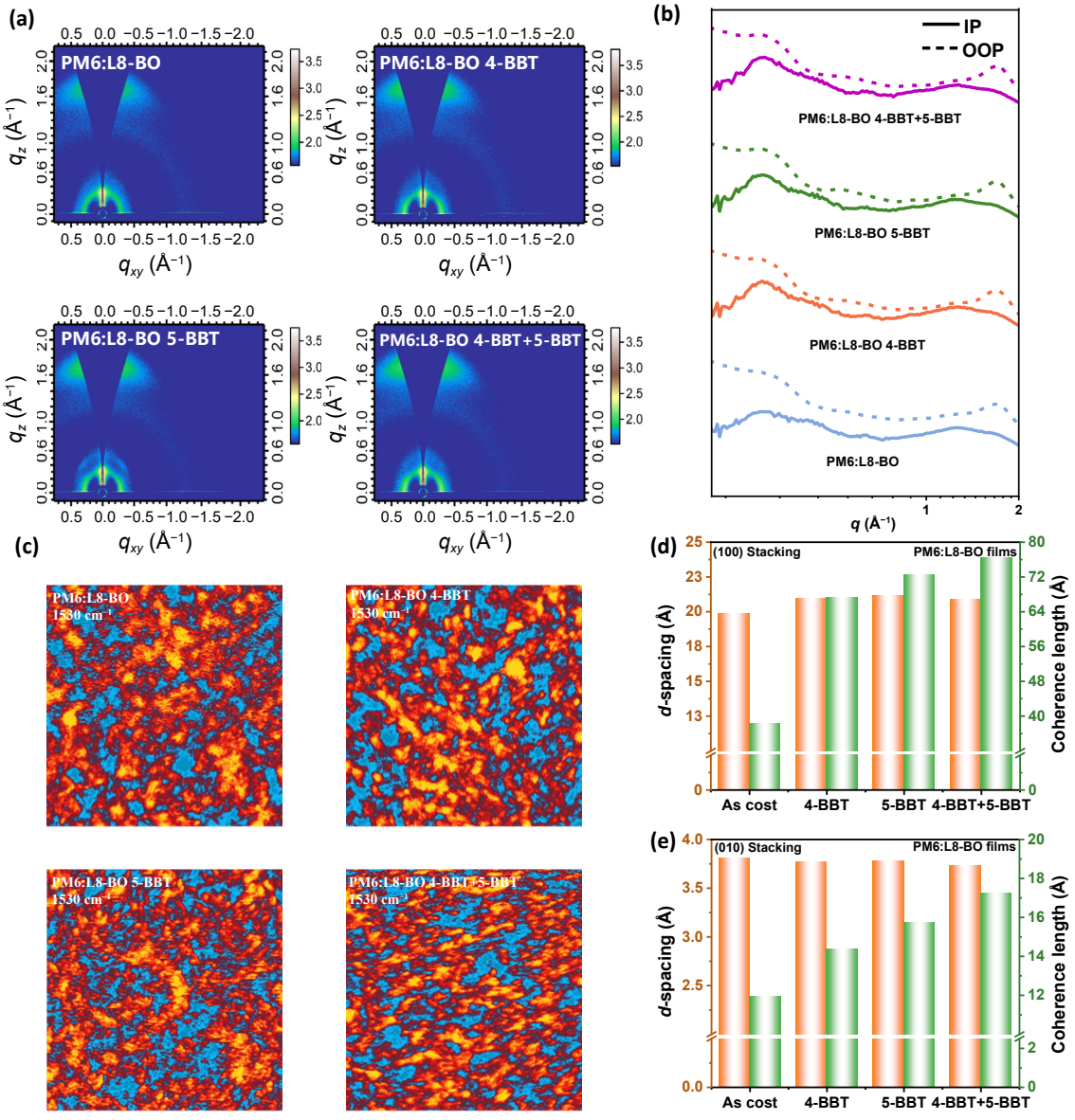

Figure 4 (a) 2D-GIWAXS patterns of the blend films in the as-cast state or treated with solid additives (4-BBT, 5-BBT, and 4-BBT+5-BBT). (b) Corresponding scattering profiles of the blend films along the IP and OOP directions. (c) AFM-IR images of the corresponding blend films without or with solid additive treatments. ((d) and (e)) Corresponding *d*-spacing, CCL values, and peak area of the blend films estimated from the (100) and (010) diffraction peaks.

photovoltaic performance of devices processed with 4-BBT+5-BBT treatment.

To further clarify the understanding of morphology evolution induced by isomeric solid additives, the nanoscale phase distribution of the blend films was visualized by utilizing AFM-IR measurement. The as-cast film without the addition exhibits relatively large domains of phase domains, which suggests their low miscibility state with each other, as reflected in Fig. 4(c). When 4-BBT or 5-BBT is introduced, the domain size is reduced and shows more uniformity, which indicates the possibility that the additive can effectively control the molecular self-organization and facilitate a more homogenous phase separation. Especially when both isomeric additives, 4-BBT and 5-BBT, are simultaneously added, the phase domains shrink into the smallest domains, accompanied by a smoother surface morphology, which can facilitate balanced charge transport and suppress molecular bimolecular recombination, corresponding to better photovoltaic performance in the dual additive devices. These observations indicate that at the nanoscale, the synergistic effects of the isomeric solid additives can enhance the device efficiency.

Next, we employed *in-situ* UV–Vis absorption spectroscopy to investigate the film formation dynamics of neat films and PM6:L8-BO blend films. Figures S7 and S8 in the ESM and Figs. 5(a)–5(c) are the time-dependent absorption spectra, two-dimensional time-resolved maps, and the temporal evolution of the maximum absorption peaks, respectively. The film formation process can be divided into three stages: initial solution absorption, molecular aggregation during solvent evaporation, and final solid-film absorption. For the neat component films, PM6 and L8-BO exhibit significantly different crystallization behaviors. In the case of PM6 in Fig. S7 in the ESM, the main absorption peak at approximately 616 nm remains relatively stable during solvent evaporation, which suggests minimal changes in aggregation. After introducing the mixed solid additives (4-BBT+5-BBT), the maximum absorption

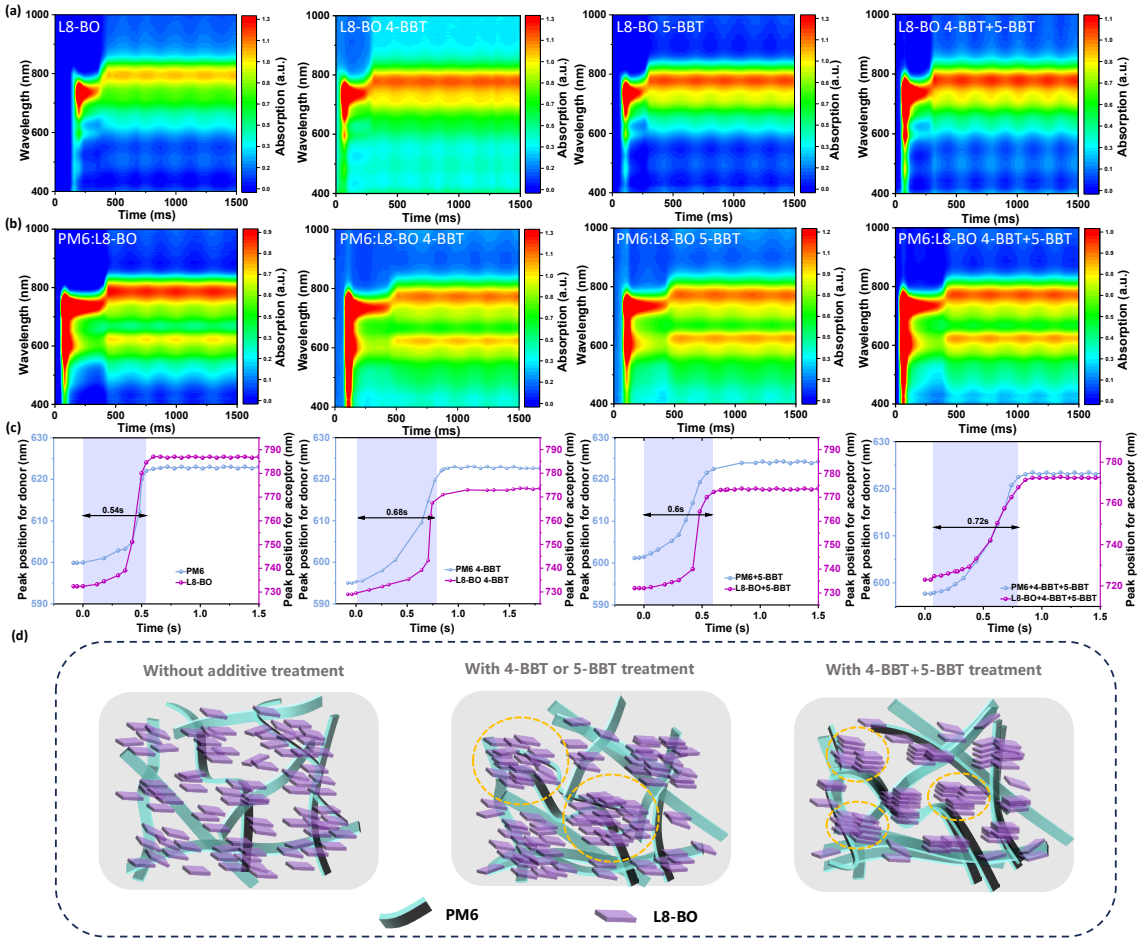

Figure 5 ((a) and (b)) 2D *in-situ* UV–Vis absorption spectra of the single-component films for (a) L8-BO and (b) blend films during film formation with or without solid additive treatments. (c) The corresponding evolution curves of the maximum absorption peak wavelengths for PM6 and L8-BO components in the blend films during film formation with or without solid additive treatments. (d) Schematic illustrations of blend morphology based on PM6:L8-BO without or with additives.

peak red-shifts to ~ 620 nm while remaining spectrally stable, which indicates enhanced molecular aggregation induced by the additives. Meanwhile, the film formation time extends from 0.48 to 0.66 s, which implies a slower crystallization process that facilitates improved molecular ordering and higher crystallinity in the PM6 film. In contrast, the L8-BO film shows a pronounced ~ 55 nm red-shift of its main absorption band at ~ 735 nm during film formation, signifying active molecular aggregation. In addition, when treated with 4-BBT+5-BBT additives, the absorption peak exhibits a ~ 16 nm blue-shift, which suggests that the additives partially intercalate into the L8-BO molecular stacks and thus weaken its intermolecular aggregation. The transition time from solution to solid state increases from 0.54 to 0.60 s after additive treatment (Fig. S8 in the ESM), implying a slower crystallization rate that allows sufficient time for nucleation and the growth of more ordered crystalline domains. The extended crystallization window promotes the formation of well-ordered molecular stacking, enhances charge transport, and reduces charge recombination.

During the film formation of PM6:L8-BO blends, the absorption dynamics of PM6 differ notably from those of the neat PM6 film. Regardless of additive treatment, a red shift of about 20 nm is observed for the PM6 absorption maximum (from 600 to 620 nm) in the blends, suggesting stronger donor aggregation induced by the donor–acceptor interactions. Compared to the neat PM6 film, the maximum absorption peak in the blend (620 nm) shifts slightly further to the red, implying that L8-BO incorporation modifies the aggregation kinetics of PM6. More strikingly, the most pronounced red shift is observed for the 4-BBT+5-BBT-treated blend, highlighting the strong aggregation-promoting capability of the mixed additives, consistent with the morphological analyses discussed above. For the L8-BO component within the blend, its maximum absorption peak gradually shifts from 720–730 to 770–790 nm during film formation. Compared to the neat L8-BO film, the blend shows a slightly blue-shifted absorption maximum, while additive-treated blends exhibit a further minor blue-shift relative to the as-cast counterpart. This behavior indicates partial additive intercalation between L8-BO molecules, similar to that observed in the neat L8-BO films. Upon additive incorporation, the overall film formation time is prolonged from 0.54 s to 0.68, 0.60, and 0.72 s, respectively. The extended nucleation and crystallization times promote the generation of abundant nucleation sites and the growth of highly ordered molecular packing, ultimately enhancing crystallinity and electronic transport.

Figure 5(d) is the schematic illustration of the morphology evolution in PM6:L8-BO blend films under different additive conditions. In the absence of additive, the L8-BO acceptor tends to over-aggregate, while PM6 chains exhibit loose packing, resulting in coarse phase domains and inefficient charge transport. The introduction of a single additive (4-BBT or 5-BBT) partially

improves molecular ordering by enhancing donor aggregation and suppressing acceptor aggregation, resulting in a moderately optimized morphology. When both isomeric additives are introduced together, a synergistic regulation of donor and acceptor aggregation is achieved, producing a finely intermixed morphology with smaller domains, improved miscibility, and well-connected transport pathways. This balanced structure facilitates efficient charge extraction and accounts for the superior device performance. Then, TA spectra around 630 nm were fitted using a segmented kinetic model to gain insight into the charge generation and relaxation dynamics in the PM6:L8-BO blend films. Corresponding 2D transient absorption spectra, femtosecond transient absorption spectra, and global fitting of kinetic traces of PM6:L8-BO-based blend films are shown in Figs. 6(a)–6(c). The kinetic curves were divided at the maximum bleach intensity, with the rising part fitted by a growth function and the decay region fitted by exponential decay functions, yielding three characteristic time constants (τ_1, τ_2, and τ_3). As shown in Table S6 in the ESM, τ_1 is the exciton dissociation or charge transfer process, τ_2 is associated with charge separation and carrier relaxation, and τ_3 corresponds to the long-lived charge recombination dynamics. For the as-cast film, τ_1, τ_2, and τ_3 were found to be 0.32, 3.57, and 368 ps, respectively, which indicates a relatively fast exciton dissociation but limited carrier lifetime. Upon introducing the 4-BBT additive, τ_1 and τ_2 increased to 0.70 and 20.7 ps, which reflects more gradual exciton–charge evolution and improved interfacial charge separation. The 5-BBT additive exhibited a slightly faster initial process (τ_1 = 0.41 ps) and a moderate τ_2 (4.99 ps), which implies less effective morphology optimization. Notably, the mixed 4-BBT+5-BBT system exhibited markedly prolonged τ_2 = 74.04 ps and extended τ_3 = 629 ps, which suggests suppressed geminate recombination and enhanced carrier lifetime. These results are consistent with the superior photovoltaic performance of the mixed-additive devices, confirming that the synergistic effect of isomeric solid additives promotes more balanced charge generation and transport dynamics. In summary, the sequential prolongation of τ_2 and τ_3 under mixed-additive treatment highlights a more favorable morphology that supports long-range charge separation and mitigates recombination losses, explaining the highest device efficiency observed in this system.

3 Conclusions

In conclusion, this work demonstrates an effective strategy for morphology modulation in high-performance OSCs via the use of isomeric solid additives 4-BBT and 5-BBT. Through the comprehensive optical, morphological, and transient characterizations, this study reveals that the cooperative incorporation of the mixed isomeric additives can synergistically suppress excessive aggregation of the L8-BO acceptor while enhancing the molecular ordering and crystallinity of the PM6 donor. In addition, the mixed 4-BBT+5-BBT system induces a more refined nanoscale phase separation with reduced domain size and improved donor–acceptor miscibility, as verified by GIWAXS and AFM-IR analyses. The optimized morphology facilitates balanced charge transport, suppressed trap-assisted recombination, and prolonged carrier lifetime, ultimately leading to a high PCE of 19.32%, along with superior J_{SC} and FF. Besides, the D18:L8-BO-C4-based devices treated with 4-BBT+5-BBT treatment delivered a remarkable PCE of 20.13%, with an outstanding FF of 83.01%. Moreover, *in-situ* UV–Vis and transient absorption studies provide dynamic insight into the film-formation and charge-transfer processes, indicating that the dual additive slows down the crystallization kinetics, promoting the formation of highly ordered molecular packing and efficient long-range charge separation. Importantly, the dual-additive device exhibits outstanding operational and thermal stability, highlighting its potential for

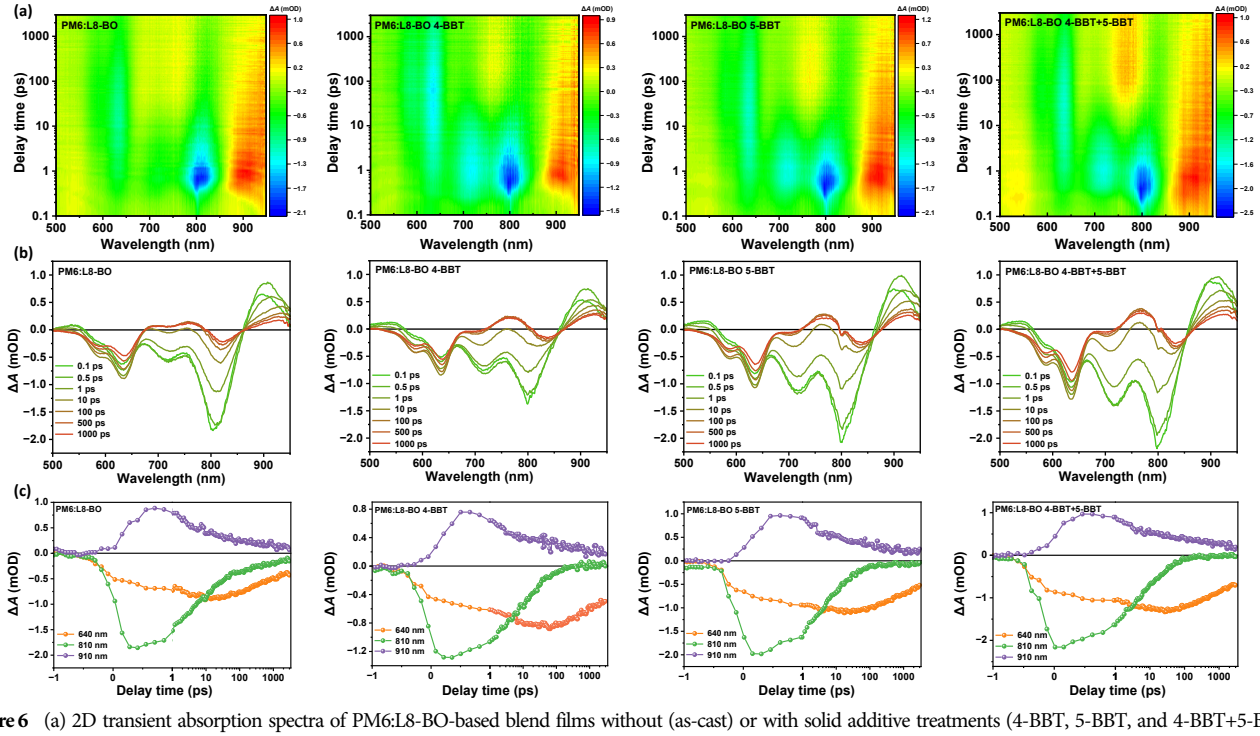

Figure 6 (a) 2D transient absorption spectra of PM6:L8-BO-based blend films without (as-cast) or with solid additive treatments (4-BBT, 5-BBT, and 4-BBT+5-BBT). (b) Corresponding femtosecond transient absorption spectra of PM6:L8-BO-based blend films at the indicated delay times. (c) Global fitting of kinetic traces of PM6:L8-BO-based blend films, probed at the indicated wavelengths.

practical photovoltaic applications. This study establishes a general and effective strategy for fine-tuning molecular aggregation and phase morphology in organic semiconductors via synergistic solid additive engineering. The insights presented herein provide valuable guidance for the rational design of multifunctional additive systems toward next-generation, high-efficiency, and stable organic solar cells.

Electronic Supplementary Material: Supplementary material (GIWAXS measurements, contact angle characterizations details and data, *in-situ* absorption spectra and data, space charge limited current and other device data) is available in the online version of this article at https://doi.org/10.26599/NR.2026.94908417.

Data availability

All data needed to support the conclusions in the paper are presented in the manuscript and the Electronic Supplementary Material. Additional data related to this paper may be requested from the corresponding author upon request.

Acknowledgement

The authors are grateful for the financial support provided by the National Natural Science Foundation of China (Nos. 52303258 and 52503289) and the Strategic Priority Research Program of the Chinese Academy of Sciences (No. XDB0770200).

Declaration of competing interest

All the contributing authors report no conflict of interests in this work.

Author contribution statement

Z. Y. Z. and D. P. R.: Data curation, project administration, validation, writing manuscript, experimental design. H. W., Z. W., and J. Q. Z.: Data curation. D. D. and Y. L. S.: Project administration. R. M. Z. and Z. X. W.: Project administration, funding acquisition, writing manuscript. All the authors have approved the final manuscript.

Use of AI statement

None.

References

[1] Li, D. H.; Deng, N.; Fu, Y. W.; Guo, C. H.; Zhou, B. J.; Wang, L.; Zhou, J.; Liu, D.; Li, W.; Wang, K. et al. Fibrillization of non-fullerene acceptors enables 19% efficiency pseudo-bulk heterojunction organic solar cells. *Adv. Mater.* **2023**, *35*, 2208211.

[2] Zeng, R.; Zhang, M.; Wang, X. D.; Zhu, L.; Hao, B. N.; Zhong, W. K.; Zhou, G. Q.; Deng, J. W.; Tan, S. K.; Zhuang, J. X. et al. Achieving 19% efficiency in non-fused ring electron acceptor solar cells via solubility control of donor and acceptor crystallization. *Nat. Energy* **2024**, *9*, 1117–1128.

[3] Sun, Y. D.; Wang, L.; Guo, C. H.; Xiao, J. Y.; Liu, C. H.; Chen, C.; Xia, W. Y.; Gan, Z. R.; Cheng, J. C.; Zhou, J. P. et al. π-extended nonfullerene acceptor for compressed molecular packing in organic solar cells to achieve over 20% efficiency. *J. Am. Chem. Soc.* **2024**, *146*, 12011–12019.

[4] Chen, Z. Y.; Ge, J. F.; Song, W.; Tong, X. Y.; Liu, H.; Yu, X. L.; Li, J.; Shi, J. Y.; Xie, L.; Han, C. C. et al. 20.2% efficiency organic photovoltaics employing a π-extension quinoxaline-based acceptor with ordered arrangement. *Adv. Mater.* **2024**, *36*, 2406690.

[5] Zhang, P. P.; Gao, N.; Du, B.; Xu, Z. G.; Wu, S. R.; Zhu, K. T.; Ma, X.; Bin, H. J.; Li, Y. F. Highly ordered polymorphism of small molecule acceptor delivering efficient and stable binary organic solar cells. *Angew. Chem., Int. Ed.* **2025**, *64*, e202424430.

[6] Zhou, Y. B.; Su, W. Y.; Liang, Z. Z.; Wu, Q.; Bai, H. R.; Liu, H.; Song, B. H.; Li, X.; Xie, B. M.; Liu, C. et al. Halogenated diphenyl ether solvent additives enable ~ 20% efficiency organic solar cells and high-performance opaque/semitransparent modules. *Natl. Sci. Rev.* **2025**, *12*, nwaf346.

[7] Liu, H.; Tang, L. T.; Li, T. F.; Yi, F.; Su, W. Y.; Xiang, K.; Dong, B. T.; Yao, Z. F.; Wang, K.; Hu, T. Y. et al. Hybrid linking sites constructed non-fully conjugated asymmetric dimerized giant molecule acceptors for organic solar cells with an efficiency of ~ 20%. *Angew. Chem., Int. Ed.* **2025**, *64*, e202503721.

[8] Zhang, M.; Zhu, L.; Zhou, G. Q.; Hao, T. Y.; Qiu, C. Q.; Zhao, Z.; Hu, Q.; Larson, B. W.; Zhu, H. M.; Ma, Z. F. et al. Single-layered organic photovoltaics with double cascading charge transport pathways: 18% efficiencies. *Nat. Commun.* **2021**, *12*, 309.

[9] Li, C.; Zhou, J. D.; Song, J. L.; Xu, J. Q.; Zhang, H. T.; Zhang, X. N.; Guo, J.; Zhu, L.; Wei, D. H.; Han, G. C. et al. Non-fullerene acceptors with branched side chains and improved molecular packing to exceed 18% efficiency in organic solar cells. *Nat. Energy* **2021**, *6*, 605–613.

[10] Cui, Y.; Xu, Y.; Yao, H. F.; Bi, P. Q.; Hong, L.; Zhang, J. Q.; Zu, Y. F.; Zhang, T.; Qin, J. Z.; Ren, J. Z. et al. Single-junction organic photovoltaic cell with 19% efficiency. *Adv. Mater.* **2021**, *33*, 2102420.

[11] Zhu, L.; Zhang, M.; Xu, J. Q.; Li, C.; Yan, J.; Zhou, G. Q.; Zhong, W. K.; Hao, T. Y.; Song, J. L.; Xue, X. N. et al. Single-junction organic solar cells with over 19% efficiency enabled by a refined double-fibril network morphology. *Nat. Mater.* **2022**, *21*, 656–663.

[12] Bai, H. R.; Su, W. Y.; Li, T. F.; Zhang, Z. Y.; Ma, R. J.; Yao, Z. F.; Xiang, K.; Maqsood, M. H.; Bi, Z. Z.; Liu, H. et al. Fullerene-embedded porphyrin metallacages as photoactive additives for stable binary organic solar cells with a certified efficiency of 20.2%. *Energy Environ. Sci.* **2025**, *18*, 10351–10363.

[13] Jørgensen, M.; Norrman, K.; Gevorgyan, S. A.; Tromholt, T.; Andreasen, B.; Krebs, F. C. Stability of polymer solar cells. *Adv. Mater.* **2012**, *24*, 580–612.

[14] Cai, Y. H.; Xie, C.; Li, Q.; Liu, C. H.; Gao, J. X.; Jee, M. H.; Qiao, J. W.; Li, Y.; Song, J. L.; Hao, X. T. et al. Improved molecular ordering in a ternary blend enables all-polymer solar cells over 18% efficiency. *Adv. Mater.* **2023**, *35*, 2208165.

[15] Qiu, B. B.; Chen, Z.; Qin, S. C.; Yao, J.; Huang, W. C.; Meng, L.; Zhu, H. M.; Yang, Y.; Zhang, Z. G.; Li, Y. F. Highly efficient all-small-molecule organic solar cells with appropriate active layer morphology by side chain engineering of donor molecules and thermal annealing. *Adv. Mater.* **2020**, *32*, 1908373.

[16] Miao, Y. W.; Sun, Y. N.; Zou, W. T.; Zhang, X.; Kan, Y. Y.; Zhang, W. Q.; Jiang, X. Y.; Wang, X. C.; Yang, R. Q.; Hao, X. T. et al. Isomerization engineering of solid additives enables highly efficient organic solar cells via manipulating molecular stacking and aggregation of active layer. *Adv. Mater.* **2024**, *36*, 2406623.

[17] Guo, L. Z.; Li, Q. D.; Ren, J. X.; Xu, Y. J.; Zhang, J. B.; Zhang, K.; Cai, Y. P.; Liu, S. J.; Huang, F. Halogenated thiophenes serve as solvent additives in mediating morphology and achieving efficient organic solar cells. *Energy Environ. Sci.* **2022**, *15*, 5137–5148.

[18] Yu, R. N.; Shi, R.; He, Z. W.; Zhang, T.; Li, S.; Lv, Q. L.; Sha, S. H.; Yang, C. H.; Hou, J. H.; Tan, Z. A. Thermodynamic phase transition of three-dimensional solid additives guiding molecular assembly for efficient organic solar cells. *Angew. Chem., Int. Ed.* **2023**, *62*, e202308367.

[19] Su, W. Y.; Zhou, X. M.; Wu, Q.; Wu, Y.; Qin, H. M.; Liang, Z. Z.; Li, H. X.; Bai, H. R.; Guo, J.; Jiang, L. et al. Halogenation engineering of solid additives enables 19.39% efficiency and stable binary organic solar cells via manipulating molecular stacking and aggregation of both donor and acceptor components. *Adv. Funct. Mater.* **2025**, *35*, 2415090.

[20] Zhu, X. W.; Gu, C. L.; Cheng, Y. T.; Lu, H.; Wang, X. L.; Ran, G. L.;

Zhang, W. K.; Tang, Z.; Bo, Z. S.; Liu, Y. H. 3D-architectured acceptor with high photoluminescence quantum yield and moderate crystallinity for high-efficiency organic solar cells with low voltage loss. *Adv. Mater.* **2025**, *37*, 2507529.

[21] Bai, Y.; Li, S. M.; Wang, Q. Y.; Chen, Q.; Zhang, Z.; Meng, S. X.; Zang, Y.; Fu, H. Y.; Xue, L. W.; Ye, L. et al. Simultaneous enhancement of efficiency, stability and stretchability in binary polymer solar cells with a three-dimensional aromatic-core tethered tetrameric acceptor. *Natl. Sci. Rev.* **2025**, *12*, nwaf019.

[22] Quiroz, Y. A. A.; Koganezawa, T.; Perkhun, P.; Barulina, E.; Ruiz, C. M.; Ackermann, J.; Yoshimoto, N.; Videlot-Ackermann, C. Exploring charge transport in high-temperature polymorphism of ITIC derivatives in simple processed unipolar bottom contact organic field-effect transistor. *Adv. Electron. Mater.* **2022**, *8*, 2100743.

[23] Purdum, G. E.; Telesz, N. G.; Jarolimek, K.; Ryno, S. M.; Gessner, T.; Davy, N. C.; Petty, A. J.; Zhen, Y. G.; Shu, Y.; Facchetti, A. et al. Presence of short intermolecular contacts screens for kinetic stability in packing polymorphs. *J. Am. Chem. Soc.* **2018**, *140*, 7519–7525.

[24] Chung, H.; Chen, S. W.; Sengar, N.; Davies, D. W.; Garbay, G.; Geerts, Y. H.; Clancy, P.; Diao, Y. Single atom substitution alters the polymorphic transition mechanism in organic electronic crystals. *Chem. Mater.* **2019**, *31*, 9115–9126.

[25] Zhao, Z. M.; Chung, S.; Kim, Y. Y.; Jeong, M.; Li, X.; Zhao, J. J.; Zhu, C. F.; Karuthedath, S.; Zhong, Y. F.; Cho, K. et al. Room-temperature-modulated polymorphism of nonfullerene acceptors enables efficient bilayer organic solar cells. *Energy Environ. Sci.* **2024**, *17*, 5666–5678.

[26] McDowell, C.; Abdelsamie, M.; Toney, M. F.; Bazan, G. C. Solvent additives: Key morphology-directing agents for solution-processed organic solar cells. *Adv. Mater.* **2018**, *30*, 1707114.

[27] Xiao, Y. Q.; Yuan, J.; Zhou, G. D.; Ngan, K. C.; Xia, X. X.; Zhu, J. S.; Zou, Y. P.; Zhao, N.; Zhan, X. W.; Lu, X. H. Unveiling the crystalline packing of Y6 in thin films by thermally induced "backbone-on" orientation. *J. Mater. Chem. A* **2021**, *9*, 17030–17038.

[28] Gutierrez-Fernandez, E.; Scaccabarozzi, A. D.; Basu, A.; Solano, E.; Anthopoulos, T. D.; Martín, J. Y6 organic thin-film transistors with electron mobilities of 2.4 $cm^2 \cdot V^{-1} \cdot s^{-1}$ via microstructural tuning. *Adv. Sci.* **2022**, *9*, 2104977.

[29] Fu, J. H.; Chen, H. Y.; Huang, P. H.; Yu, Q. Q.; Tang, H.; Chen, S. S.; Jung, S.; Sun, K.; Yang, C.; Lu, S. R. et al. Eutectic phase behavior induced by a simple additive contributes to efficient organic solar cells. *Nano Energy* **2021**, *84*, 105862.

[30] Song, J. L.; Zhu, L.; Li, C.; Xu, J. Q.; Wu, H. B.; Zhang, X. N.; Zhang, Y.; Tang, Z.; Liu, F.; Sun, Y. M. High-efficiency organic solar cells with low voltage loss induced by solvent additive strategy. *Matter* **2021**, *4*, 2542–2552.

[31] Zeng, R.; Zhu, L.; Zhang, M.; Zhong, W. K.; Zhou, G. Q.; Zhuang, J. X.; Hao, T. Y.; Zhou, Z. C.; Zhou, L. B.; Hartmann, N. et al. All-polymer organic solar cells with nano-to-micron hierarchical morphology and large light receiving angle. *Nat. Commun.* **2023**, *14*, 4148.

[32] Cui, Y.; Yao, H. F.; Zhang, J. Q.; Zhang, T.; Wang, Y. M.; Hong, L.; Xian, K. H.; Xu, B. W.; Zhang, S. Q.; Peng, J. et al. Over 16% efficiency organic photovoltaic cells enabled by a chlorinated acceptor with increased open-circuit voltages. *Nat. Commun.* **2019**, *10*, 2515.

[33] Sun, Y. Q.; Chung, S.; Huang, X. D.; Cho, K.; Kan, Z. P. Suppressing nongeminate recombination with two well-compatible polymer donors enables 16.6% efficiency all-polymer solar cells. *Chem. Eng. J.* **2023**, *470*, 144186.

[34] Zhan, L. L.; Li, S. X.; Li, Y. K.; Sun, R.; Min, J.; Bi, Z. Z.; Ma, W.; Chen, Z.; Zhou, G. Q.; Zhu, H. M. et al. Desired open-circuit voltage increase enables efficiencies approaching 19% in symmetric-asymmetric molecule ternary organic photovoltaics. *Joule* **2022**, *6*, 662–675.

[35] Pang, B.; Liao, C. T.; Xu, X. P.; Yu, L. Y.; Li, R. P.; Peng, Q. Benzo[d]thiazole based wide bandgap donor polymers enable 19.54% efficiency organic solar cells along with desirable batch-to-batch reproducibility and general applicability. *Adv. Mater.* **2023**, *35*, 2300631.

[36] Zhao, J. J.; Chung, S.; Li, H. X.; Zhao, Z. M.; Zhu, C. F.; Yin, J.; Cho, K. L.; Kan, Z. P. Impact of intermolecular interactions between halogenated volatile solid additives and the nonfullerene acceptor in organic solar cells. *Adv. Funct. Mater.* **2023**, *33*, 2307355.

[37] Fan, B. B.; Zhong, W. K.; Gao, W.; Fu, H. T.; Lin, F. R.; Wong, R. W. Y.; Liu, M.; Zhu, C. H.; Wang, C.; Yip, H. L. et al. Understanding the role of removable solid additives: Selective interaction contributes to vertical component distributions. *Adv. Mater.* **2023**, *35*, 2302861.

[38] Peng, Z. X.; Ye, L.; Ade, H. Understanding, quantifying, and controlling the molecular ordering of semiconducting polymers: From novices to experts and amorphous to perfect crystals. *Mater. Horiz.* **2022**, *9*, 577–606.

[39] Hung, K. E.; Lin, Y. S.; Xue, Y. J.; Yang, H. R.; Lai, Y. Y.; Chang, J. W.; Su, C. J.; Su, A. C.; Hsu, C. S.; Jeng, U. S. et al. Non-volatile perfluorophenyl-based additive for enhanced efficiency and thermal stability of nonfullerene organic solar cells via supramolecular fluorinated interactions. *Adv. Energy Mater.* **2022**, *12*, 2103702.

[40] Ge, Z. W.; Qiao, J. W.; Li, Y.; Song, J. L.; Zhang, C.; Fu, Z.; Jee, M. H.; Hao, X. T.; Woo, H. Y.; Sun, Y. M. Over 18% efficiency of all-polymer solar cells with long-term stability enabled by Y6 as a solid additive. *Adv. Mater.* **2023**, *35*, 2301906.

[41] Liu, L.; Kan, Y. Y.; Gao, K.; Wang, J. X.; Zhao, M.; Chen, H.; Zhao, C. J.; Jiu, T.; Jen, A. K. Y.; Li, Y. L. Graphdiyne derivative as multifunctional solid additive in binary organic solar cells with 17.3% efficiency and high reproductivity. *Adv. Mater.* **2020**, *32*, 1907604.

[42] Wang, Y. F.; Liang, Z. Z.; Liang, X. F.; Wen, X. M.; Cai, Z. Z.; Shao, Z. M.; Zhang, J. B.; Ran, Y. X.; Yan, L. H.; Lu, G. H. et al. Easy isomerization strategy for additives enables high-efficiency organic solar cells. *Adv. Energy Mater.* **2023**, *13*, 2300524.

[43] Wang, J. Q.; Wang, Y. F.; Bi, P. Q.; Chen, Z. H.; Qiao, J. W.; Li, J. Y.; Wang, W. X.; Zheng, Z.; Zhang, S. Q.; Hao, X. T. et al. Binary organic solar cells with 19.2% efficiency enabled by solid additive. *Adv. Mater.* **2023**, *35*, 2301583.

[44] Fan, Q. P.; Ma, R. J.; Yang, J.; Gao, J. S.; Bai, H. R.; Su, W. Y.; Liang, Z. Z.; Wu, Y.; Tang, L. X.; Li, Y. X. et al. Unidirectional sidechain engineering to construct dual-asymmetric acceptors for 19.23% efficiency organic solar cells with low energy loss and efficient charge transfer. *Angew. Chem., Int. Ed.* **2023**, *62*, e202308307.

[45] Song, X.; Xu, H.; Jiang, X. Y.; Gao, S. Z.; Zhou, X. J.; Xu, S. L.; Li, J. J.; Yu, J.; Liu, W. Z.; Zhu, W. G. et al. Film-formation dynamics coordinated by intermediate state engineering enables efficient thickness-insensitive organic solar cells. *Energy Environ. Sci.* **2023**, *16*, 3441–3452.

[46] Cowan, S. R.; Roy, A.; Heeger, A. J. Recombination in polymer-fullerene bulk heterojunction solar cells. *Phys. Rev. B* **2010**, *82*, 245207.

[47] Gautam, P.; Misra, R.; Siddiqui, S. A.; Sharma, G. D. Unsymmetrical donor–acceptor–acceptor–π–donor type benzothiadiazole-based small molecule for a solution processed bulk heterojunction organic solar cell. *ACS Appl. Mater. Interfaces* **2015**, *7*, 10283–10292.